Available online at www.sciencedirect.com
ScienceDirect
Journal of Magnetic Resonance 182 (2006) 84–95
JMR Journal of Magnetic Resonance
www.elsevier.com/locate/jmr

Polar Fourier transforms of radially sampled NMR data

Brian E. Coggins, Pei Zhou *

Department of Biochemistry, Duke University Medical Center, Durham, NC 27710, USA

Received 5 April 2006; revised 2 June 2006
Available online 3 July 2006

Abstract

Radial sampling of the NMR time domain has recently been introduced to speed up data collection significantly. Here, we show that radially sampled data can be processed directly using Fourier transforms in polar coordinates. We present a comprehensive theoretical analysis of the discrete polar Fourier transform, and derive the consequences of its application to radially sampled data using linear response theory. With adequate sampling, the resulting spectrum using a polar Fourier transform is indistinguishable from conventionally processed spectra with Cartesian sampling. In the case of undersampling in azimuth—the condition that provides significant savings in measurement time—the correct spectrum is still produced, but with limited distortion of the baseline away from the peaks, taking the form of a summation of high-order Bessel functions. Finally, we describe an intrinsic connection between the polar Fourier transform and the filtered backprojection method that has recently been introduced to process projection-reconstruction NOESY data. Direct polar Fourier transformation holds great potential for producing quantitatively accurate spectra from radially sampled NMR data.

Keywords: Polar Fourier transform; Radial sampling

1. Introduction

In recent years, a number of multidimensional NMR techniques have been proposed that share in common the sampling of the time domain along radial spokes [1–16], an approach that has been termed *radial sampling* [17]. The conventional procedure for multidimensional experiments, which consists of sampling the time domain on a Cartesian grid, requires measurement times that can become significant for the three- or more dimensional experiments that constitute the foundation of modern biomolecular NMR. The drive for increased throughput in studies of small biomolecules, as well as the demand for experiments with more dimensions and higher resolution in studies of large biomolecules, have together motivated the exploration of alternative approaches.

Sampling the time domain along radial spokes is synonymous with coevolving two or more indirect dimensions of an experiment, a procedure related to the historical *accordion spectroscopy* [2], and which has become common recently in the form of the *reduced dimensionality* (RD) experiments and their more recently introduced cousins, the GFT experiments [3–7,11,18]. Customarily, these RD/GFT experiments would measure a single radial slice along the diagonal of the time domain, which would be Fourier transformed to give a lower dimensional spectrum, with peak positions determined as linear combinations of the frequencies in the jointly sampled dimensions. The *projection spectroscopy* methods develop this sampling further, by measuring multiple radial slices of the time domain, at different angles, which are each Fourier transformed independently to yield a set of projection spectra [8–10,12–16]. The projection interpretation is a powerful one, and has lead to a variety of methods for utilizing the radially sampled data, which can be classified into those that compute reconstructions of the full higher-dimensional spectrum from the lower-dimensional projections [8–10,12,13,16,19], and those that analyze the peak positions on the projections directly [14,15,20].

* Corresponding author. Fax: +1 919 684 8885.
E-mail address: peizhou@biochem.duke.edu (P. Zhou).

1090-7807/$ - see front matter © 2006 Elsevier Inc. All rights reserved.
doi:10.1016/j.jmr.2006.06.016

An interesting question is whether radially sampled NMR data could be processed directly with a multidimensional Fourier transform (FT), yielding a *quantitative* higher-dimensional spectrum determined according to the familiar properties of the FT. Noting that the sampling procedure used in the projection spectroscopy method is essentially a sampling in polar coordinates, we turned to forms of the discrete FT that operate in a polar domain, which we refer to collectively as the polar FT (PFT). Here, we evaluate the unique properties of the polar FT, and consider in detail its application to radially sampled NMR data.

When our study was completed, we learned of a parallel effort by Kazimierczuk and coworkers, now recently published [21], involving the computation of spectra from both radially and spirally-sampled data, using the traditional equation for the discrete FT (DFT). Our work has focused specifically on the radial case, to obtain a comprehensive understanding of its qualities. Additionally, our PFT equations point to an oversight in the previous DFT work: There is a need to correct for the unequal area density of the sampling pattern, in order to obtain quantitative peak lineshapes.

In this article, we derive analytical expressions governing the spectra obtained for discrete NMR data, providing a theoretical understanding of the numerical and experimental results reported previously for the radial case. An important result is the determination that it is possible to obtain spectra that are virtually identical to those generated by discrete FTs of data sampled on Cartesian grids. We further discuss a connection between polar Fourier transforms and the filtered backprojection method for quantitative reconstruction from projections.

2. Theory

2.1. Notation

Throughout this paper, lower-case variables represent functions and coordinates in the NMR time domain, while upper-case letters represent the same for the NMR frequency domain. We denote a Fourier transform pair using a double-headed arrow

$$f(x) \Longleftrightarrow F(X). \tag{1}$$

Convolution is indicated with an asterisk,

$$f(x) * g(x) \equiv \int_{-\infty}^{\infty} f(u)g(x-u)\,\mathrm{d}u, \tag{2}$$

which is readily extended to multiple dimensions. The function $\Pi(x)$ is the rectangular cutoff

$$\Pi(x) \equiv \begin{cases} 1 & |x| < 1/2, \\ 1/2 & |x| = 1/2, \\ 0 & |x| > 1/2. \end{cases} \tag{3}$$

Its Fourier transform is the sinc function, defined to be

$$\operatorname{sinc} x \equiv \frac{\sin \pi x}{\pi x}. \tag{4}$$

The function $\delta_{2\text{-D}}(x,y)$ represents the Dirac delta function in 2-D

$$\delta_{2\text{-D}}(x,y) \equiv \begin{cases} 1 & x,y = 0, \\ 0 & x \text{ or } y \neq 0. \end{cases} \tag{5}$$

We follow Bracewell [22] in using $\delta_{2\text{-D}}$ of a single variable to designate a delta function dependent only on the one variable, that is, a line impulse. For example

$$\delta_{2\text{-D}}(x) = \begin{cases} 1 & x = 0, \\ 0 & x \neq 0 \end{cases} \tag{6}$$

describes an infinitely sharp impulse along the y-axis. The direction of an impulse $\delta_{2\text{-D}}(u)$ is always normal to the direction described by u. Note also that $\delta_{2\text{-D}}(x,y) = \delta_{2\text{-D}}(x)\,\delta_{2\text{-D}}(y)$.

An infinite 1-D train of impulses spaced at integer increments in x is the pulse train function III

$$\mathrm{III}(x) \equiv \sum_{i=-\infty}^{\infty} \delta(x-i). \tag{7}$$

In discussions of delta functions and other functions that do not have conventional integrals, the generalized function interpretation of an integral in the limit is assumed [22,23].

2.2. Continuous radial polar transforms

The starting point for our discussions will be the conventional Cartesian Fourier transform of a continuous 2-D complex-valued function $f(x,y)$

$$F(X,Y) = \int_{-\infty}^{\infty}\int_{-\infty}^{\infty} f(x,y)\mathrm{e}^{-2\pi\mathrm{i}(xX+yY)}\,\mathrm{d}x\,\mathrm{d}y. \tag{8}$$

One approach to calculate a spectrum would be to evaluate this equation directly for the known sampling points, with the rest of the domain implicitly assumed to be zero [21]. This could be used for radial data. However, it is reasonable to ask whether changing Eq. (8) to polar coordinates would give additional insight into the situation.

Substituting $r = \sqrt{x^2+y^2}$ and $\theta = \arctan\, y/x$, and changing the differentials $\mathrm{d}x\,\mathrm{d}y$ to $r\,\mathrm{d}r\,\mathrm{d}\theta$, Eq. (8) becomes the continuous transform of a radially sampled function [24,25]:

$$F(X,Y) = \int_0^{2\pi}\int_0^{\infty} f(r,\theta)\mathrm{e}^{-2\pi\mathrm{i}r(X\cos\theta+Y\cos\theta)} r\,\mathrm{d}r\,\mathrm{d}\theta, \tag{9}$$

where $0 \leqslant \theta < 2\pi$ and $0 \leqslant r < \infty$.

The primary difference between Eqs. (9) and (8) is the factor r in the change of differentials, which corrects for the unequal area density of sampling points in the radial pattern. Without this correction, each infinitesimal area element defined by $\mathrm{d}r\,\mathrm{d}\theta$ would be given uniform weighting, even though the sizes of these elements are not uniform over the whole plane. This has more general implications

for FT processing of data sampled on non-Cartesian patterns, which we will discuss in detail below.

The fact that we represent F in Cartesian coordinates in Eq. (9), despite changing f to polar coordinates, is worthy of comment. Although it is possible to calculate F in a polar space, it is important to recognize that the Fourier transform always produces equal information about F for all points in the X/Y plane, regardless of the coordinate system of the input function f. We conclude that the evenly distributed Cartesian grid is better suited than a polar grid for reporting the transform results.

As written in Eq. (9), the transform is evaluated first with respect to r, and second with respect to θ. We shall refer to this form of the polar FT as a *radial* transform. This equation fits naturally with the interpretation of the 2-D FT kernel as a superposition of 1-D cosine and sine waves in all directions [22,26]; here, each spoke of $f(r,\theta)$ at fixed θ contributes the weighting coefficients for the cosine and sine waves in direction θ used in the synthesis of F (Fig. 1). Since the specific position along a kernel wave in direction θ for a point $F(X, Y)$ can be located with a frequency domain radial coordinate $R' = X\cos\theta + Y\cos\theta$, we can write

$$F(X,Y) = \int_0^{2\pi}\int_0^{\infty} f(r,\theta)\mathrm{e}^{-2\pi i r R'} r\,\mathrm{d}r\,\mathrm{d}\theta \tag{10}$$

showing that the innermost integration is essentially a 1-D FT with respect to r. Letting F_r represent the data following this integration, we find that F_r is entirely in the frequency domain, and that the kernel has been evaluated completely. All that remains is a simple integration of F_r along θ. This is in contrast to the standard Cartesian approach of separating the kernel into x and y components, where following transformation over one variable, the kernel component for the other variable still remains.

2.3. Continuous azimuthal polar transforms

It is also possible to compute transforms in which the harmonic kernel components vary as θ [25,27–29], and the innermost integration is a 1-D FT with respect to θ. We shall refer to these transforms as *azimuthal*. The intention in the azimuthal transform is to fit $f(r,\theta)$ with waves that travel about circular rings of various radii r, with n periods per ring (Figs. 2a and b). Naturally, n will be

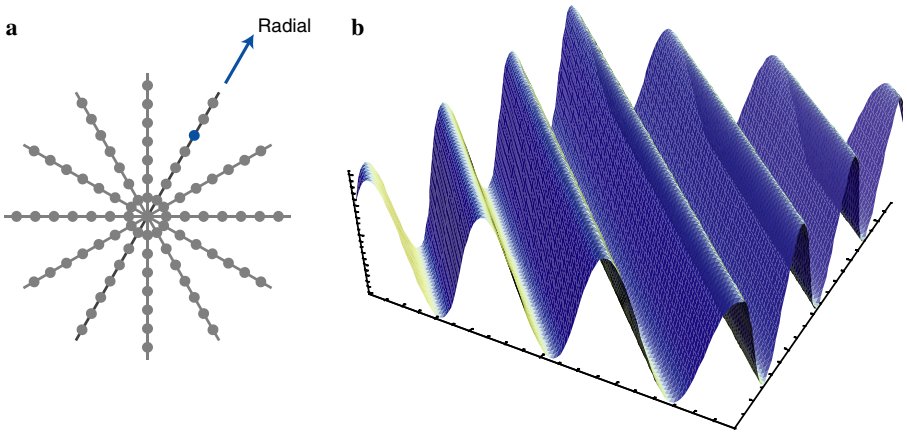

Fig. 1. Radial form of the polar FT. (a) In the radial form, the transform is computed with respect to the radial coordinate r. (b) The synthesis is formed from waves in all directions and of all radial frequencies. The amplitude of a single wave (blue) in F is determined by the value of a corresponding point in f (blue point in a), with the frequency determined by the distance of the point from the origin.

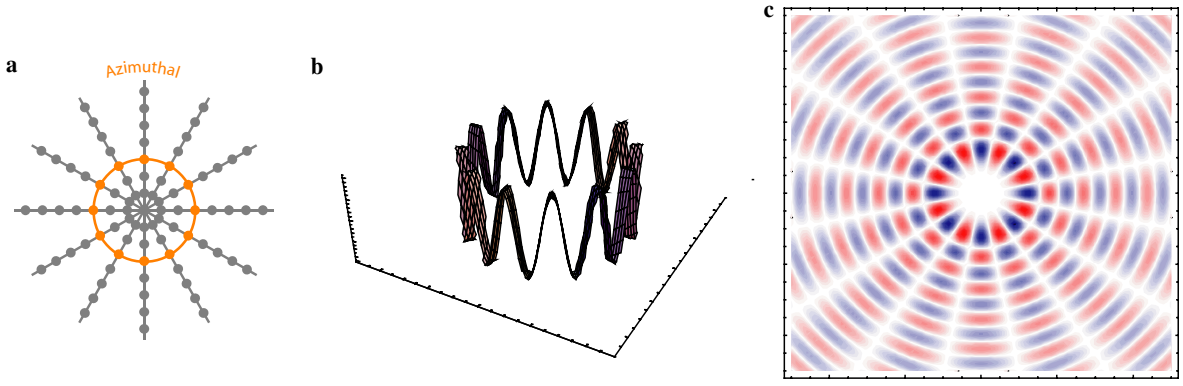

Fig. 2. Azimuthal form of the polar FT. (a) In the azimuthal form, the transform is evaluated with respect to θ. (b) The *degree of fit* between a wave of period n about the ring and the data f determines the weighting coefficient for a synthesis term of order n. (c) The n-order synthesis term, shown as a contour plot with positive contours in blue and negative contours in red, varies as an n-order Bessel function of R and as sinusoids of n cycles with Θ.

limited to integers. Eq. (9) can be rearranged so that the innermost integration is over θ

$$\begin{aligned} F(X,Y) &= \int_0^\infty \int_0^{2\pi} f(r,\theta) e^{-2\pi i r(X\cos\theta + Y\sin\theta)} r\,d\theta\,dr \\ &= \int_0^\infty \int_0^{2\pi} f(r,\theta) e^{-2\pi i r(R\cos\Theta\cos\theta + R\sin\Theta\sin\theta)} r\,d\theta\,dr \\ &= \int_0^\infty \int_0^{2\pi} f(r,\theta) e^{-2\pi i r R\cos(\theta-\Theta)} r\,d\theta\,dr, \end{aligned} \tag{11}$$

where we introduce $R = \sqrt{X^2+Y^2}$ and $\Theta = \arctan Y/X$. Using the following relation [29]:

$$e^{iu\cos\phi} = \sum_{n=-\infty}^{\infty} i^n J_n(u) e^{in\phi}, \tag{12}$$

where J_n is the Bessel function of order n, taking $u = 2\pi rR$ and $\phi = \theta - \Theta$, we derive

$$F(X,Y) = \int_0^\infty \int_0^{2\pi} \sum_{n=-\infty}^{\infty} f(r,\theta) i^n J_n(2\pi rR) e^{in(\Theta-\theta)} r\,d\theta\,dr. \tag{13}$$

Eq. (13) can be rearranged as

$$F(X,Y) = \int_0^\infty \sum_{n=-\infty}^{\infty} \left[\int_0^{2\pi} f(r,\theta) e^{-in\theta}\,d\theta\right] i^n J_n(2\pi rR) e^{in\Theta} r\,dr. \tag{14}$$

The integral in brackets is a 1-D Fourier transform with respect to θ. This transform over θ explicitly analyzes f into harmonic components of θ, indexed by their integer angular frequencies n (Fig. 2b). The amplitudes of the harmonic components in this transform provide weighting coefficients for the components used in the final synthesis of F, which vary with Θ as sinusoids and with R as Bessel functions of various orders. An example of one of these components is plotted in Fig. 2c.

The azimuthal and radial transforms are equivalent methods for calculating the continuous polar 2-D Fourier transform. For practical NMR signal processing, it is advantageous to adopt the radial transform, as it can be evaluated as a 1-D transform with respect to r followed by an integration, while the azimuthal involves a 1-D transform with respect to θ followed by the summation of a series of Bessel function terms. Additionally, the radial transform can be conveniently extended to hyperdimensional spaces, simply by changing the weighting factor r and integrating over the additional angles. However, extending the azimuthal transforms to higher-dimensional functions requires introducing spherical or even higher-dimensional polar harmonics. Nevertheless, we find the azimuthal transform to be a useful analytical tool for predicting the consequences of limited sampling in the azimuthal coordinate for 2-D functions.

2.4. NMR data and discrete transforms

Several additional considerations must be addressed before the calculation of spectra from NMR data are possible using the above equations. First, the multidimensional NMR time domain is normally observed as hypercomplex rather than complex data, i.e., letting $f_x(x)$ and $f_y(y)$ represent the signals arising from the evolution of nuclei in x and y, respectively, four hypercomplex observations are made:

$$\begin{aligned} I_1(r,\theta) &= \mathrm{Re}[f_x(r\cos\theta)]\mathrm{Re}[f_y(r\sin\theta)], \\ I_2(r,\theta) &= \mathrm{Re}[f_x(r\cos\theta)]\mathrm{Im}[f_y(r\sin\theta)], \\ I_3(r,\theta) &= \mathrm{Im}[f_x(r\cos\theta)]\mathrm{Re}[f_y(r\sin\theta)], \\ I_4(r,\theta) &= \mathrm{Im}[f_x(r\cos\theta)]\mathrm{Im}[f_y(r\sin\theta)], \end{aligned} \tag{15}$$

rather than the two complex components $\mathrm{Re}[f(r,\theta)]$ and $\mathrm{Im}[f(r,\theta)]$ needed in Eq. (9). By inserting a factor i for each imaginary component measured, we obtain the desired complex data as a linear combination of the observations:

$$\begin{aligned} f(r,\theta) &= \frac{1}{2}(\mathrm{Re}[f_x(r\cos\theta)]\mathrm{Re}[f_y(r\sin\theta)] \\ &\quad - \mathrm{Im}[f_x(r\cos\theta)]\mathrm{Im}[f_y(r\sin\theta)]) \\ &\quad + \frac{i}{2}(\mathrm{Re}[f_x(r\cos\theta)]\mathrm{Im}[f_y(r\sin\theta)] \\ &\quad + \mathrm{Im}[f_x(r\cos\theta)]\mathrm{Re}[f_y(r\sin\theta)]) \\ &= \frac{1}{2}(I_1 - I_4) + \frac{i}{2}(I_2 + I_3). \end{aligned} \tag{16}$$

NMR signals are *causal*, meaning that observations can only be made for the $+x$ $+y$ quadrant, corresponding to positive evolution times. The Fourier transformation of a complex dataset populated only for the $+x$ $+y$ quadrant—as generated by Eq. (16)—leads to mixed-phase or "phase-twist" lineshapes, due to the superposition of dispersive and absorptive components [30]

$$\mathrm{Re}[F_{+x+y}(X,Y)] = \mathrm{Re}[F_x]\mathrm{Re}[F_y] - \mathrm{Im}[F_x]\mathrm{Im}[F_y], \tag{17}$$

In order to obtain purely absorptive lineshapes, we employ a mirror-image reflection of the $+x$ $+y$ data into the $-x$ $+y$ quadrant, while taking the complex conjugate with respect to x. This procedure is closely related to the time-reversal method used historically in 2D J spectroscopy [30]. The reflection is computed using the linear combination

$$\begin{aligned} f(r,\pi-\theta) &= \frac{1}{2}(\mathrm{Re}[f_x(r\cos\theta)]\mathrm{Re}[f_y(r\sin\theta)] \\ &\quad + \mathrm{Im}[f_x(r\cos\theta)]\mathrm{Im}[f_y(r\sin\theta)]) \\ &\quad + \frac{i}{2}(\mathrm{Re}[f_x(r\cos\theta)]\mathrm{Im}[f_y(r\sin\theta)] \\ &\quad - \mathrm{Im}[f_x(r\cos\theta)]\mathrm{Re}[f_y(r\sin\theta)]) \\ &= \frac{1}{2}(I_1 + I_4) + \frac{i}{2}(I_2 - I_3). \end{aligned} \tag{18}$$

Since $\bar{g}(-u) \Longleftrightarrow \overline{G}(U)$, the transform of the reflected $-x+y$ data alone also has a phase-twist shape, but with the signs of the phase-twist lobes reversed

$$\mathrm{Re}[F_{-x+y}(X,Y)] = \mathrm{Re}[F_x]\mathrm{Re}[F_y] + \mathrm{Im}[F_x]\mathrm{Im}[F_y]. \tag{19}$$

Combining the original data (Eq. (16)) and the reflected data (Eq. (18)) and computing the FT, the dispersive components cancel, and a purely absorptive lineshape is obtained. The $-y$ half of the time domain is left at zero to preserve causality in the final transform, ensuring that $\mathrm{Im}[F(X,Y)]$ is the Hilbert transform of $\mathrm{Re}[F(X,Y)]$ and may be discarded, as with conventional spectra [31].The discrete transform could be calculated at this point by direct evaluation of Eq. (9) or (10), but it is computationally more efficient to calculate the inner integral as a 1-D FFT with respect to r. The limits of Eq. (10) are first changed

$$F(X,Y) = \int_0^{\pi}\int_{-\infty}^{\infty} f(r,\theta)\mathrm{e}^{-2\pi i r R'}|r|\,\mathrm{d}r\,\mathrm{d}\theta, \tag{20}$$

so that each radial spoke includes negative r evolution times, corresponding to the $-y$ half of the plane, supplied in practice by twofold zero filling along each radial vector. After computing the FFT for spokes in directions $0 \leqslant \theta \leqslant \pi$, one has an intermediate dataset F_r, sampled for discrete positions of the R' coordinate. The final summation over θ requires interpolation to a Cartesian grid, carried out here as previously described for PR purposes [32]. The proper resolution for the discrete X/Y grid is determined by the maximum evolution time $r_{\max}$.

2.5. Point response functions

Having defined the forms of the polar transform, we now consider the behavior of this transform for discrete data. Linear response theory, which was used extensively in the development of pulsed NMR, provides a powerful framework for understanding the consequences of any discrete sampling method [22,23,30]. We are interested in characterizing how the spectrum produced by a transform of discrete radially sampled data differs from the true spectrum of the continuous signal.

Discrete sampling methods can be treated as linear systems that operate on a theoretically continuous input to yield the actual, observed output [22,24,25]

$$F_{\Psi}(X,Y) = \Psi[F(X,Y)], \tag{21}$$

where Ψ represents the action of the sampling filter to generate the output spectrum F_{Ψ} from a signal with true spectrum F. The result of Ψ can be determined for any input if we know the characteristic *point response* of Ψ

$$H_{\Psi}(X,Y) = \Psi[\delta_{2\text{-D}}(X,Y)], \tag{22}$$

which is the response to an input that is an infinitely sharp point signal [22,23,25,30]. The point response is often called the "point-spread function," because it describes how the process Ψ *spreads* the infinitely sharp *point* into a finite image. The foundation of response theory is that if the impulse response is known, the output of the system can be calculated for any arbitrary input [22,23,30]

$$F_{\Psi}(X,Y) = F(X,Y) * H_{\Psi}(X,Y). \tag{23}$$

While our goal is to understand the effects of the sampling process on the final result in the frequency domain, the actual sampling for NMR happens in the time domain. The sampling process is equivalent to multiplying the continuous signal by a sampling function $s(r,\theta)$, which is one for any value that is sampled, and zero otherwise, and then taking the (continuous) Fourier transform:

$$\Psi[F(X,Y)] \equiv \int_0^{\pi}\int_{-\infty}^{\infty} f(r,\theta)s(r,\theta)\mathrm{e}^{-2\pi i r R'}|r|\,\mathrm{d}r\,\mathrm{d}\theta. \tag{24}$$

The point response H_{Ψ} is then:

$$\begin{aligned} H_{\Psi}(X,Y) &= \Psi[\delta_{2\text{-D}}(X,Y)] \\ &= \int_0^{\pi}\int_{-\infty}^{\infty} s(r,\theta)\mathrm{e}^{-2\pi i r R'}|r|\,\mathrm{d}r\,\mathrm{d}\theta = S(X,Y), \end{aligned} \tag{25}$$

where we have used the Fourier transform pair $\delta_{2\text{-D}}(X,Y) \Longleftrightarrow 1$. Thus the point response function H_{Ψ} is nothing more than the transform $S(X,Y)$ of the sampling function s, indicating that it is in fact the sampling pattern that directly determines the manner and extent of variation from the true spectrum.

2.6. Point response functions for discrete sampling in azimuth

We now consider the effects of discrete radial sampling, by defining a suitable s and computing its FT. The most salient characteristic of the NMR sampling pattern as practiced to date is limited sampling in θ. This characteristic has permitted the enormous time savings over conventional sampling, and it is the consequences of this limited sampling that are most important for assessing the results of Fourier transforming this data into a spectrum. By comparison, the sampling in r is on par with conventional approaches, and its discreteness should have much less impact on the result.

Given these facts, it is thus interesting to consider a sampling function s_N which is discrete in θ, but continuous in r. This function can be defined in Cartesian and polar coordinates as:

$$\begin{aligned} s_N(x,y) &= \sum_{i=1}^{N} \delta_{2\text{-D}}(x\sin\varphi_i + y\cos\varphi_i), \\ s_N(r,\theta) &= \sum_{i=1}^{N} \delta_{2\text{-D}}(r\cos\theta\sin\varphi_i + r\sin\theta\cos\varphi_i), \end{aligned} \tag{26}$$

where N radial spokes are measured for directions from 0 to π (i.e., following processing by Eqs. (16) and (18)), the azimuth value for a given spoke i denoted as φ_i. It is assumed that the spokes are distributed evenly in θ. The radial PFT of this sampling function is then

$$S_N(X,Y) = \sum_{i=1}^{N} \int_{-\infty}^{\infty} \delta_{2\text{-D}}(r\cos\theta\sin\varphi_i + r\sin\theta\cos\varphi_i)\mathrm{e}^{-2\pi i r R'}|r|\,\mathrm{d}r. \quad (27)$$

It is convenient to represent this transform as the summation of an intermediate result

$$S_N(X,Y) = \sum_{i=1}^{N} S_{N,r}(R',\theta), \quad (28)$$

where $S_{N,r}$ can be written, using the convolution theorem and the FT pair $\delta_{2\text{-D}}(x) \Longleftrightarrow \delta_{2\text{-D}}(Y)$ [22], as

$$S_{N,r}(R',\theta) = \delta_{2\text{-D}}(R'\cos\theta\sin(\varphi_i+\frac{\pi}{2}) + R'\sin\theta\cos(\varphi_i+\frac{\pi}{2})) * \int_{-\infty}^{\infty} |r|\mathrm{e}^{-2\pi i r R'}\,\mathrm{d}r. \quad (29)$$

However, the transformation of the weighting function $|r|$ at the end of Eq. (29) poses a problem, as it does not converge. To resolve this, Eq. (29) must be modified to impose a cutoff on r of $r_{\max}$, beyond which $r = 0$ [24,25,33]. Using the rectangular cutoff Π of Eq. (3), the latter integral then becomes

$$\int_{-\infty}^{\infty} \Pi\left(\frac{r}{2r_{\max}}\right)|r|\mathrm{e}^{-2\pi i r R'}\,\mathrm{d}r = 2r_{\max}\ \mathrm{sinc}\ 2r_{\max}R' - r_{\max}\mathrm{sinc}^2 r_{\max}R', \quad (30)$$

and the frequency domain intermediate result follows:

$$S_{N,r}(R',\theta) = \delta_{2\text{-D}}\left(R'\cos\theta\sin\left(\varphi_i+\frac{\pi}{2}\right) + R'\sin\theta\cos\left(\varphi_i+\frac{\pi}{2}\right)\right) * (2r_{\max}\ \mathrm{sinc}\ 2r_{\max}R' - r_{\max}\ \mathrm{sinc}^2 r_{\max}R'). \quad (31)$$

A numerical simulation of the point response for $N = 25$ is plotted in Fig. 3a. The point response that we have derived is the superposition of a contribution for each radial spoke. A radial spoke in direction θ_i contributes a set of ridges in the direction $\theta_i + \pi/2$, with the overall shape defined by Eq. (30). As one might expect, increasing the cutoff $r_{\max}$, representing an increase in the radial resolution, leads to a sharpening of the contribution in each sampled direction; in the limit of infinite r, the point response becomes the superposition of line impulses normal to the time domain sampling directions. The final pattern could be described in a simplified way as an "aster" or "star" pattern with N spokes, but this does not take into account many details of the response, including the disappearance of the spokes, and their replacement by symmetric ripples, for R coordinates below a cutoff.

It is perhaps more informative to consider an alternative formulation of the point response. Instead of treating s as the sum of N continuous spokes cut off at $r_{\max}$, we can consider s to be the integration for radii up to $r_{\max}$ of rings with radius r' each sampled N times over the range of 0 to π

$$s_N(r,\theta) = \int_0^{r_{\max}} \delta(r-r')(N/\pi)\mathrm{III}(\theta N/\pi)\,\mathrm{d}r'. \quad (32)$$

The cutoff at $r_{\max}$ is required for the same reason as the rectangular cutoff in Eq. (30), so that integration of the weighting factor r in a polar FT will converge. The azimuthal FT of this function is then calculated by first taking a 1-D transform with respect to θ for a given radius r (Fig. 2) [29]:

$$S_{N,\theta}(r,n) = \int_0^{2\pi} (N/\pi)\mathrm{III}(\theta N/\pi)\mathrm{e}^{-in\theta}d\theta = 2N\mathrm{III}(n/2N). \quad (33)$$

The transform $\mathrm{III}(n/2N)$ indicates that the $2N$ delta functions per ring of the sampling function can be synthesized from a series of waves around the ring, with frequencies that are integer multiples of the fundamental frequency $2N$. This can then be substituted into Eq. (14) to give

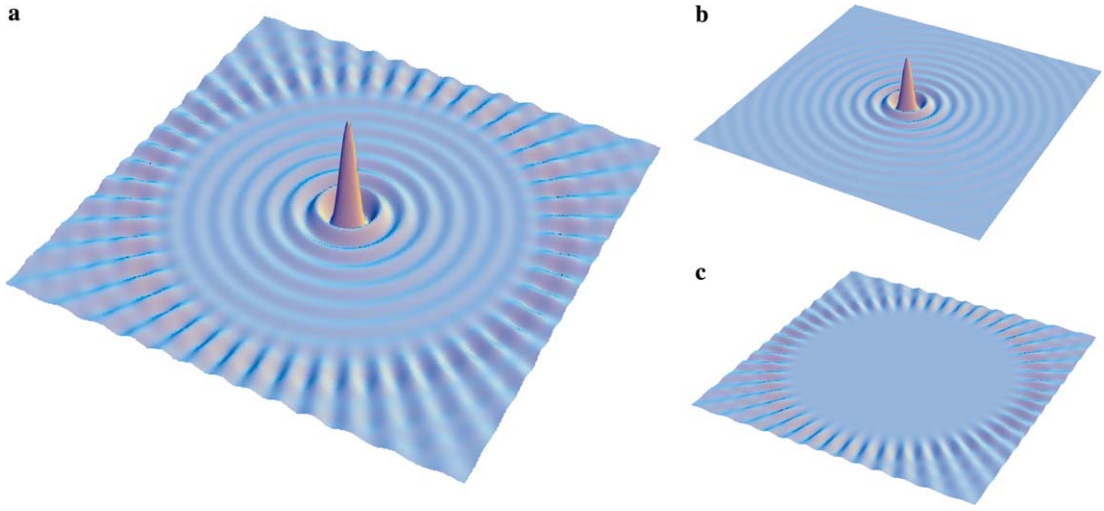

Fig. 3. Point response functions for discrete radial sampling. (a) The point response function S_N for $N = 25$. (b) The circularly symmetric J_0 term of the point response, which becomes J_1 following integration. This term arises from truncation of the signal in the radial dimension r. (c) The spoke pattern generated by the higher-order terms of the point response (here, for $N = 25$). This spoke pattern contains a clear zone without artifacts, the size of which is predicted analytically. This is the observed pattern of artifacts for a signal that is not truncated in r.

$$S_N(X,Y) = \int_0^{r_{\max}} \sum_{n=-\infty}^{\infty} i^n J_n(2\pi rR) e^{in\Theta} r\,dr, \quad n = 0, \pm 2N, \pm 4N \ldots, \tag{34}$$

where the effect of the sampling function $\mathrm{III}(n/2N)$ in Eq. (33) is to select the orders of n that contribute to S_N [24,27–29]. This result is identical to Eq. (31), although in a very different form, and is plotted in Fig. 3a.

In this second form, the point response is seen as the superposition of Bessel functions of different orders. The J_0 term can be integrated separately to give

$$\int_0^{r_{\max}} rJ_0(2\pi rR)\,dr = \frac{r_{\max}}{2\pi R} J_1(2\pi r_{\max} R). \tag{35}$$

This term is circularly symmetric, and produces the ripples that spread away from the central peak (Fig. 3b). This pattern is identical to the famous Airy diffraction pattern encountered routinely in optics [26]. As $r_{\max}$ is increased, the ripples become smaller and more closely spaced, and the central peak narrows. In the limit of sampling $r_{\max}$ to infinity, the integral of the J_0 term becomes the delta function $\delta_{2\text{-D}}(0,0)$, and the central ripples vanish.

The other terms of the series vary with respect to R as Bessel functions of higher orders, and with respect to Θ as sinusoidal functions. These terms generate the spoke pattern seen in the point response for R beyond a cutoff (Fig. 3c). All of these terms have frequencies about the ring that are integer multiples of the fundamental frequency $2N$, arising from having $2N$ points about each ring in the time domain. Because a Bessel function $J_n(u)$ has a value very close to zero for $u < n$, each term J_n likewise is very close to zero for $2\pi rR < n$ [24,28,29]. We can thus infer that:

$$\int_0^{r_{\max}} \sum_{n=\pm 2N}^{\infty} i^n J_n(2\pi rR) e^{in\Theta} r\,dr \approx 0, \quad R < N/\pi r_{\max}. \tag{36}$$

This explains why the spoke pattern in the point response is only present for R above a cutoff radius: that cutoff is $N/\pi r_{\max}$, which defines the distance from the origin at which the lowest-order Bessel functions of the spoke response, J_{2N} and J_{-2N}, become active. Increasing the radial resolution cutoff $r_{\max}$ moves this cutoff closer to the origin; increasing the number of sampling points N moves it farther from the origin. The dependence on N defines the azimuthal analog of resolution.

2.7. Point response function for discrete sampling in the radial coordinate

The derivation of the point response S_N intentionally ignored the discreteness of r for the sake of clarity, but this can easily be introduced. The form of Eq. (31) changes slightly (ignoring normalization):

$$S_{N,r,\text{discrete}}(R',\theta) = \mathrm{III}\left(\frac{R'}{\Delta r}\cos\theta \sin\left(\varphi_i + \frac{\pi}{2}\right) + \frac{R'}{\Delta r}\sin\theta\cos\left(\varphi_i + \frac{\pi}{2}\right)\right) * \left(2r_{\max}\mathrm{sinc}2r_{\max}R' - r_{\max}\mathrm{sinc}^2 r_{\max}R'\right) \tag{37}$$

Rather than a single ridge, the point response for each direction is now a series of ridges in the same direction $\theta_i + \pi/2$, replicated at the regular spacing $1/\Delta r$. Assuming that the radial spectral width is set correctly, these replications will occur beyond the limits of the spectrum, and will not affect the observed result. This equation shows that the discrete polar FT is actually periodic in both r and θ; however, in general this does *not* lead to the regular periodicity in X and Y found with the Cartesian DFT. Note that it is therefore not possible to fold peaks intentionally in a PFT spectrum, since intentional aliasing is facilitated by the periodicity of the Cartesian point response.

In order to avoid intrusion of the radial signal replications into the spectrum, we adjust Δr for each spoke, as described previously [10]. In this case, the correct values of r must be used in reweighting the sampling points on each spoke; it is also necessary to scale the FFT output for each spoke after the transform over r, according to the similarity theorem of the FT, since the FFT does not take into account the different point spacings on the spokes. Additionally, note that for the same number of points on each spoke, the maximum evolution times will be different in different directions, which should theoretically lead to a truncation of the signals in the diagonal directions. In practice, the truncation effects are of a very low level, and appear beneath the noise in experimental spectra.

3. Results

To demonstrate the application of the polar Fourier transform to NMR, we present both the results of numerical simulation, and experimental data. We first compare simulation results (Fig. 4) for a zero-frequency Lorentzian peak of 128 Hz linewidth in a spectrum of 2000 Hz width on each axis, sampled and processed using (a) Cartesian sampling with 64 complex points per axis and the conventional DFT, (b) radial sampling with 64 complex points in r and $N = 128$ samples in θ, followed by a radial PFT, and (c) radial sampling with 64 complex points in r and $N = 32$ samples in θ. The latter two would correspond to 64 and 16 observed radial spokes, respectively, prior to reflection of the data by Eq. (18). The conventional and $N = 128$ radially sampled spectra are essentially identical and show no artifacts. The $N = 32$ radially sampled spectrum is undersampled in θ, and contains the spoke pattern of the higher-order Bessel function series found in the radial sampling point response. Because the signal reaches zero before the end of each radial FID, the J_1 ripple artifacts, which arise from truncation in r, are not generated.

These simulation results are consistent with experimental data from a 3-D HNCO spectrum on the 19 kDa OTU protein (Fig. 5). Two N/CO planes are shown, one containing a single peak (top panel), and the other containing six (bottom panel). Four spectra are compared, (1) a standard Cartesian-sampled spectrum with 52×52 time domain sampling points (red traces), (2) the radial FT result for 48 measured radial spokes ($N = 96$ after reflec-

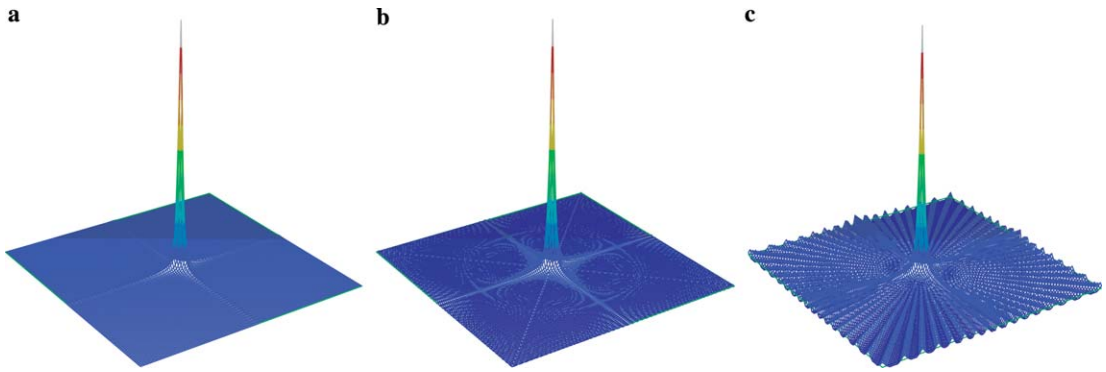

Fig. 4. Simulations of Cartesian and polar Fourier transforms. (a) The discrete Cartesian FT of a simulated Lorentzian peak. (b) The discrete radial polar FT of the same simulated Lorentzian peak, for $N = 128$ radial samples, each with 64 complex points in r. This transform correctly reproduces the Lorentzian peak of (a), with a slight vertical offset due to the zeroing of the point at $f(0,0)$ by the radial weighting function r, and with <0.1% baseline fluctuation due to limited numerical precision in the integration over θ. (c) The discrete radial polar FT of the same peak, for $N = 32$ radial samples. The spoke pattern arising from the higher-order Bessel terms in the point response is visible, extending almost to the base of the peak. The spokes are not of identical shape due to the convolution with the peak shape.

tion), each with 52 points (green traces), (3) the conventional spectrum for 25×25 sampling points (purple traces) and (4) the radial FT spectrum for 12 radial spokes ($N = 24$ after reflection) (blue traces). For clarity, the positions of the sampling points in the time domain for each dataset have been plotted in Supplementary Figure S1. These spectra compare Cartesian and radial results for two roughly equal numbers of sampling points, (1) and (2) having 2704 and 2496 points, respectively, and (3) and (4) having 625 and 624 points, respectively. The right side of the figure features N and CO 1-D cross-sections through some of the peaks [(b) and (d)].

As with the simulation, the conventional 52×52 point and 48 radial spoke results are essentially identical. The results with limited sampling show the consequences of the sampling pattern: The 625 point Cartesian spectrum has broadened peaks, while the peaks in the 12 radial spoke ($N = 24$) spectrum remain sharp, at the expense of picking up the J_{48} Bessel spoke artifact pattern that is characteristic of undersampling in θ. This spoke pattern is of a low level by comparison to the peaks, but is still quite significant. The sensitivity in both ~625 point spectra is reduced from that of the ~2500 point cases due to the decreased signal averaging.

The experimental and simulation results confirm the accuracy of the theoretical predictions. We were able to reproduce the Cartesian results within the measurement error, using radial sampling and polar transforms. In addition, in cases of undersampling, both simulation and experiment reproduced the higher-order Bessel function point response, as an artifact pattern corrupting the baseline away from the peaks.

4. Discussion

4.1. Corrections for the area density of sampling points

The theoretical treatment of the polar FT leads to a more general conclusion about FT processing of data sampled on non-Cartesian patterns. The proper conversion of the continuous FT (Eq. (8)) to a general discrete equation for an arbitrary sampling pattern is

$$F_{\mathrm{DFT}}(X,Y) = \sum_i f(x_i,y_i)\mathrm{e}^{-2\pi\mathrm{i}(x_iX+y_iY)}\Delta A_i, \tag{38}$$

where a sampling point i at a position (x_i, y_i) has a weight ΔA_i, reflecting the area it occupies in the x/y plane. In constrast with Kazimierczuk et al. [21], ΔA_i may only be ignored for Cartesian sampling; in a general case it must be determined, ideally analytically, but if necessary by empirical methods such as the Voronoi diagram [34].

In the radial case, the proper weighting can be obtained analytically as $\Delta A_i = r_i \Delta r \Delta\theta$, which simplifies to r_i as long as Δr and $\Delta\theta$ are uniform (and in fact, when we vary Δr to prevent aliasing, as described above, an additional correction must be made for the unequal Δr for different spokes). It has been shown for the FT processing of radially sampled imaging data that computing the transform without this weighting factor leads to a convolution between the true image (here, spectrum) and the function $1/R$ [24]:

$$F_{\mathrm{uncorrected}}(X,Y) = F(X,Y) * \frac{1}{R}, \tag{39}$$

which results in a severe broadening of all peaks, due to the overemphasis of low frequency components in the synthesis of $F_{\mathrm{uncorrected}}$. For other unevenly distributed sampling patterns, like the recently proposed spiral approach [21], it will be important to determine the appropriate weighting factors to produce accurate peak lineshapes.

4.2. Lineshapes, artifacts, and time savings

Much of the recent interest in radial sampling has been driven by the prospect of obtaining spectra in less measurement time than would be necessary with conventional

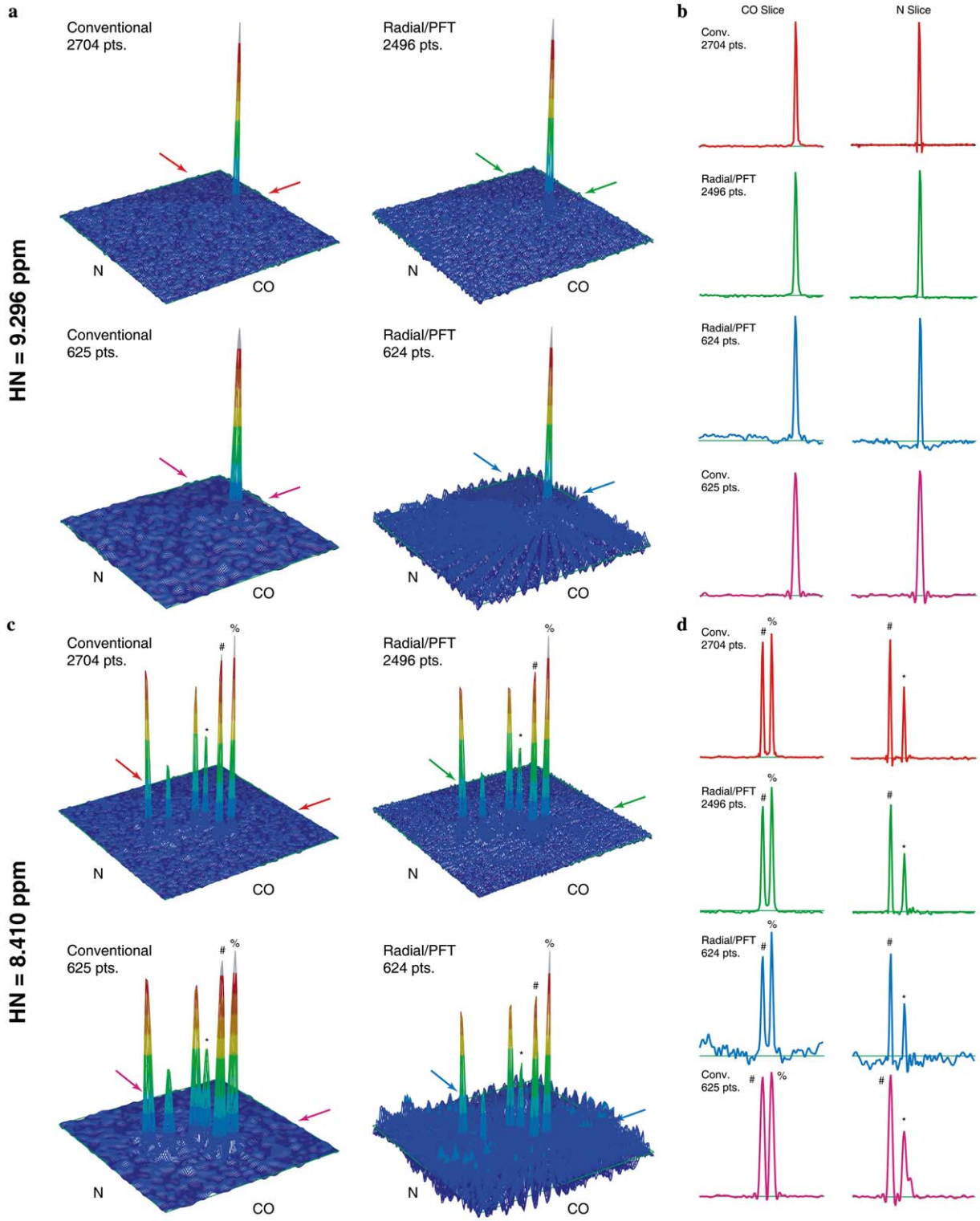

Fig. 5. Comparison of Cartesian and radial sampling for experimental data. Two N/CO planes from the 3-D HNCO spectrum of the 19 kDa OTU protein are shown, at HN chemical shifts of 9.296 and 8.410 ppm for the top and bottom panels, respectively. Stacked plots are given for conventional Cartesian-sampled data with 2704 (52×52) or 625 (25×25) sampling points, processed by the conventional DFT, and for radially sampled data with 2496 (48 spokes, 52 points each) or 624 points (12 spokes, 52 points each), processed by the radial form of the polar FT. At right are 1-D cross-sections in the N and CO directions passing through some of the peaks; the positions of the cross-sections are indicated by color-coded arrows on the stacked plots. Peak identification in (d) is indicated with the symbols *, #, and %. (a) A plane containing a single peak. Full sampling produces essentially identical spectra, whether by the Cartesian or radial pattern. Undersampling of the conventional data leads to a loss of resolution, while undersampling of the radial data results in baseline artifacts assuming the spoke pattern of the J_{48} Bessel function. (b) Cross-sections through the same. (c) A plane containing six peaks. All six peaks are reproduced with the correct shapes and relative intensities in all spectra. (d) Cross-sections show accurate peak reproduction, but in the radially-undersampled case, there are also significant baseline artifacts.

methods. There has been some concern, however, about the accuracy of spectra reconstructed from radial projections.

The results of this study confirm analytically that it is possible to obtain a quantitatively accurate spectrum from radially sampled data, if those data are processed using a PFT, and if the degree of sampling is sufficient. Such spectra are equivalent to those obtained conventionally, within the error caused by noise and limited precision in the calculations. Because the method is an FT, the effects of relaxation and apodization on lineshapes is the same as with conventional data collection. Sensitivity is proportional to the number of measurements, since the same signal-averaging rules apply as in any FT. Two opposed factors influence the observed sensitivity: the increased sampling near the origin should increase signal levels over Cartesian sampling with the same number of data points, at least for decaying signals; however, the reweighting of the data points in the polar transform equation would counteract this. The consequences for the noise level and the resulting signal-to-noise ratio are not entirely clear, and are an area for further study.

We have also shown that it is possible to calculate a spectrum from a small number of radial samples, at the expense of baseline artifacts following spoke patterns. The observed spectrum is a convolution between the true spectrum and the point response of the sampling process, with the consequence that the artifact pattern is replicated for each peak in the spectrum, centered on the peak, and scaled according to the size and shape of the peak. With radial sampling, at a given resolution, there is a tradeoff between artifacts and measurement time, as dictated by Eq. (36). While the artifacts may be problematic for experiments with a large dynamic range—such as NOESY experiments with diagonal peaks—in cases where time is of the essence, accurate peak shapes are important, and a limited amount of artifacts are acceptable, a significant savings in time may be realized by reducing the sampling in θ, without leading to a loss of resolution. However, in the extreme of a *very* small number of radial spokes, the artifacts will begin to overlap with the peaks, resulting in peak distortion.

It should also be noted that since the sampling pattern directly determines the artifact pattern (Eq. (23) or (25)), it might be possible to design other sampling patterns with a more favorable balance between artifacts, resolution and measurement time. Spiral sampling is an example of a pattern that has been shown to generate reduced artifact levels by comparison with the radial approach [21]. However, it also important to ensure that any new patterns reproduce peak shapes accurately, as we have shown is the case for radial sampling. There is also great potential for the application of non-linear methods to deconvolute the artifact pattern [19]; the analytical understanding of the artifact pattern given here may facilitate this.

4.3. Connections to projection methods

There is a surprisingly close connection between the polar FT and the filtered backprojection method described in the literature. Consider the 1-D FT of a radial spoke in f in a given direction θ

$$F_p(R,\theta) = \int_{-\infty}^{\infty} f(r,\theta) e^{-2\pi i r R}\, dr, \tag{40}$$

for $0 \leqslant \theta < \pi$ and $-\infty < r < \infty$. According to the projection-slice theorem of the Fourier transform [1,22,35–37], $F_p(R,\theta)$ is the projection of F at angle θ, that is, the integration of F along lines at angles $\theta + \pi/2$

$$F_p(R,\theta) = \int_{-\infty}^{\infty} F(R\cos\theta - S\sin\theta, R\sin\theta + S\cos\theta)\, dS. \tag{41}$$

Many of the current efforts to determine NMR spectra from radially sampled data have focused on the idea of inverting Eq. (41), to obtain F from F_p. A variety of methods have been described for carrying out this inversion for NMR data [9,10,13,16,17,38,39], and even more methods have been described in the literature of other scientific fields [24,25,28,33,35–37,40–44].

A popular method in the imaging community, which was recently demonstrated for NMR [13], is *filtered backprojection* (FBP) [24,25,33,36,37,42,44]. FBP is the analytical inversion of Eq. (41), and can be represented as:

$$F(X,Y) = \int_0^{\pi} \int_{-\infty}^{\infty} \left[\int_{-\infty}^{\infty} F_P(R',\theta)\, e^{2\pi i r R'} dR' \right] \times e^{-2\pi i r (X\cos\theta + Y\cos\theta)} |r|\, dr\, d\theta. \tag{42}$$

This method involves (1) inverse transformation of F_p, (2) filtering by a filter function $|r|$, (3) forward transformation to give a "modified projection" or "filtered projection," and (4) integration over θ, which is termed "backprojection." Eq. (42) bears a striking similarity to the radial form of the polar FT. In fact, after the transformation of F_p to f, *the two methods are identical*. We see that the intermediate result F_r defined for the radial FT is the same as the "filtered projections" of FBP, and that the final integration over θ in Eq. (10) is the same operation as "backprojection." The FBP process can be summarized as

$$F_p \xrightarrow{\text{1-D FT}^{-1}} f \xrightarrow{|r|;\text{1-D FT}} F_r \xrightarrow{\text{backprojection}} F, \tag{43}$$

which we now see is the same as

$$F_p \xrightarrow{\text{1-D FT}^{-1}} f \xrightarrow{\text{radial PFT}} F. \tag{44}$$

This result highlights the strong connections between Fourier transforms and the various phenomena of projections. When the physically observed data are F_p, as in imaging applications, the net process that must be performed is the reconstruction of F from projections. Accurate reconstructions can be calculated by first transforming into the time domain, and then computing a polar

Fourier synthesis. Normally a radial synthesis is employed, and the net process is called FBP, although the azimuthal transform of Eq. (14) could also be used, as with DeRosier and Klug's determination of the structure of bacteriophage T4 from electron micrographs [41].

In NMR, the physically observed data are f, not F_p, and the process to obtain F from radially sampled f need not be anything more than a polar Fourier transform:

$$f \xrightarrow{\text{radial PFT}} F \tag{45}$$

Performing FBP on NMR data implicitly includes calculating a radial PFT, following a detour to generate projection data F_p:

$$f \xrightarrow{\text{1-D FT}} F_p \xrightarrow{\text{1-D FT}^{-1}} f \xrightarrow{\text{radial PFT}} F. \tag{46}$$

4.4. Hyperdimensional polar fourier transforms

The radial form of the polar FT described here for 2-D can easily be extended to d dimensions, by using the appropriate change of differentials to convert from the d-dimensional Cartesian space to the d-dimensional polar space. This would typically require a weighting function of r^{d-1} multiplied by a function accounting for the azimuthal distribution about the hypersphere. As in the 2-D case, the kernel is evaluated during the innermost integration over r, with the remaining operations being a simple summation of values over the azimuthal space.

5. Conclusions

Radially sampled data can be processed by a specifically polar FT to yield quantitative spectra; we have presented a comprehensive theoretical treatment of the process and results, which correctly predicts the behavior of the polar transform for discretely sampled data. The polar FT equations point to the need for a corrective factor when applying DFT calculations to unequally distributed sampling patterns, to account for the uneven area density of the sampling. The theory shows that the discrete PFT gives nearly identical results to the conventional FT, provided that sufficient samples are available in θ. When θ is undersampled, as a method for reducing measurement time, the resulting spectrum shows the correct peaks with the correct sizes and shapes, but with the baseline corrupted by a spoke pattern. These theoretical results have been confirmed by simulations and experiment. Direct transformation of data from radial and perhaps other sampling patterns is an intriguing area for further development, with great potential for NMR.

6. Methods

NMR data were collected on a Varian INOVA 600 MHz spectrometer, equipped with a triple-resonance probe with Z-axis gradients. A 3 mM $^{13}C/^{15}N/^{2}H$-labeled sample of OTU, in 25 mM sodium phosphate buffer, with 100 mM KCl, 2 mM DTT, and 5% D_2O, was used, and experiments were conducted at 25 °C. The spectral width was 1900 Hz on each indirect axis, and 8000 Hz for the directly observed proton axis. A TROSY-HNCO pulse sequence was used for both experiments, modified appropriately to support radial sampling. The conventional experiment recorded 52 complex points for each indirect axis, in 26 h. In the radially sampled experiment, 48 radial spokes were measured at equal azimuthal increments of 1.91°, with 52 complex points in the radial dimension, in 24 h. The spectral widths of the radial spokes were adjusted to prevent aliasing as previously described [10]. The sampling patterns are plotted explicitly in Supplementary Figure S1.

Data were initially processed in NMRPipe [45]. The $N = 24$ dataset was formed from the $N = 96$ dataset by selecting every fourth radial spoke. The 25×25 point conventional dataset was prepared by truncating the 52×52 measured data. Each reduced dataset is equivalent to a 6 h experiment. All data were apodized by cosine functions in the N and CO dimensions. Conventional spectra were zero-filled to twice the initial length; radial spokes were processed as described in Sections 2.4 and 2.7 above. Radial transforms were calculated using PR-CALC [32].

Acknowledgments

We thank Ms. Martha Bomar for supplying the sample of OTU. This work was supported by the Whitehead Institute and by N.I.H. Grant AI055588-01 to P.Z. B.E.C. is the recipient of an N.S.F. Graduate Research Fellowship.

Appendix A. Supplementary data

Supplementary data associated with this article can be found, in the online version, at doi:10.1016/j.jmr.2006.06.016.

References

[1] K. Nagayama, P. Bachmann, K. Wüthrich, R.R. Ernst, The use of cross-sections and of projections in two-dimensional NMR spectroscopy, J. Magn. Reson. 31 (1978) 133–148.
[2] G. Bodenhausen, R.R. Ernst, The accordion experiment, a simple approach to three-dimensional spectroscopy, J. Magn. Reson. 45 (1981) 367–373.
[3] T. Szyperski, G. Wider, J.H. Bushweller, K. Wuthrich, 3D ^{13}C–^{15}N-heteronuclear two-spin coherence spectroscopy for polypeptide backbone assignments in ^{13}C–^{15}N-double-labeled proteins, J. Biomol. NMR 3 (1993) 127–132.
[4] J.P. Simorre, B. Brutscher, M.S. Caffrey, D. Marion, Assignment of NMR spectra of proteins using triple-resonance two-dimensional experiments, J. Biomol. NMR 4 (1994) 325–334.
[5] K. Ding, A.M. Gronenborn, Novel 2D triple-resonance NMR experiments for sequential resonance assignments of proteins, J. Magn. Reson. 156 (2002) 262–268.
[6] W. Kozminski, I. Zhukov, Multiple quadrature detection in reduced dimensionality experiments, J. Biomol. NMR 26 (2003) 157–166.

[7] S. Kim, T. Szyperski, GFT NMR, a new approach to rapidly obtain precise high-dimensional NMR spectral information, J. Am. Chem. Soc. 125 (2003) 1385–1393.
[8] R. Freeman, E. Kupče, New methods for fast multidimensional NMR, J. Biomol. NMR 27 (2003) 101–113.
[9] E. Kupče, R. Freeman, Reconstruction of the three-dimensional NMR spectrum of a protein from a set of plane projections, J. Biomol. NMR 27 (2003) 383–387.
[10] B.E. Coggins, R.A. Venters, P. Zhou, Generalized reconstruction of n-D NMR spectra from multiple projections: application to the 5-D HACACONH spectrum of protein G B1 domain, J. Am. Chem. Soc. 126 (2004) 1000–1001.
[11] Y. Xia, G. Zhu, S. Veeraraghavan, X. Gao, (3,2)D GFT-NMR experiments for fast data collection from proteins, J. Biomol. NMR 29 (2004) 467–476.
[12] R. Freeman, E. Kupče, Distant echoes of the accordion: reduced dimensionality, GFT-NMR, and projection-reconstruction of multidimensional spectra, Concepts Magn. Res. 23A (2004) 63–75.
[13] B.E. Coggins, R.A. Venters, P. Zhou, Filtered backprojection for the reconstruction of a high-resolution (4,2)D CH3-NH NOESY spectrum on a 29 kDa protein, J. Am. Chem. Soc. 127 (2005) 11562–11563.
[14] S. Hiller, F. Fiorito, K. Wüthrich, G. Wider, Automated projection spectroscopy, Proc. Natl. Acad. Sci. USA 102 (2005) 10876–10881.
[15] H.R. Eghbalnia, A. Bahrami, M. Tonelli, K. Hallenga, J.L. Markley, High-resolution iterative frequency identification for NMR as a general strategy for multidimensional data collection, J. Am. Chem. Soc. 127 (2005) 12528–12536.
[16] D. Malmodin, M. Billeter, Multiway decomposition of NMR spectra with coupled evolution periods, J. Am. Chem. Soc. 127 (2005) 13486–13487.
[17] E. Kupče, R. Freeman, Fast multidimensional NMR: radial sampling of evolution space, J. Magn. Reson. 173 (2005) 317–321.
[18] T. Szyperski, G. Wider, J.H. Bushweller, K. Wuthrich, Reduced dimensionality in triple-resonance NMR experiments, J. Am. Chem. Soc. 115 (1993) 9307–9308.
[19] J.W. Yoon, S. Godsill, E. Kupče, R. Freeman, Deterministic and statistical methods for reconstructing multidimensional NMR spectra, Magn. Reson. Chem. 44 (2006) 197–209.
[20] D. Malmodin, M. Billeter, Signal identification in NMR spectra with coupled evolution periods, J. Magn. Reson. 176 (2005) 47–53.
[21] K. Kazimierczuk, W. Kozminski, I. Zhukov, Two-dimensional Fourier transform of arbitrarily sampled NMR data sets, J. Magn. Reson. 179 (2006) 323–328.
[22] R.N. Bracewell, The Fourier Transform and Its Applications, McGraw-Hill, Boston, 2000.
[23] R.J. Beerends, H.G. ter Morsche, J.C. van den Berg, E.M. van de Vrie, Fourier and Laplace Transforms, Cambridge University Press, Cambridge, 2003.
[24] P.F.C. Gilbert, The reconstruction of a three-dimensional structure from projections and its application to electron microscopy. II. Direct methods, Proc. R. Soc. Lond. B 182 (1972) 89–102.
[25] A.R. Thompson, R.N. Bracewell, Interpolation and Fourier transformation of fringe visibilities, Astron. J. 79 (1974) 11–24.
[26] R.N. Bracewell, Two-Dimensional Imaging, Prentice-Hall, Englewood Cliffs, NJ, 1995.
[27] W. Cochran, F.H.C. Crick, V. Vand, The structure of synthetic polypeptides. I. The transform of atoms on a helix, Acta Cryst. 5 (1952) 581.
[28] A. Klug, F.H.C. Crick, H.W. Wyckoff, Diffraction by helical structures, Acta Cryst. 11 (1958) 199.
[29] J. Waser, Fourier transforms and scattering intensities of tubular objects, Acta Cryst. 8 (1955) 142.
[30] R.R. Ernst, G. Bodenhausen, A. Wokaun, Principles of Nuclear Magnetic Resonance in One and Two Dimensions, Clarendon Press, Oxford, 1987.
[31] J.C. Hoch, A.S. Stern, NMR Data Processing, Wiley-Liss, New York, 1996.
[32] B.E. Coggins, P. Zhou, PR-CALC: a program for the reconstruction of NMR spectra from projections, J. Biomol. NMR 34 (2006) 179–195.
[33] R.N. Bracewell, A.C. Riddle, Inversion of fan-beam scans in radio astronomy, Astrophys. J. 150 (1967) 427–434.
[34] M. Bourgeois, F.T.A.W. Wajer, D. Dvan Ormondt, D. Graveron-Demilly, Reconstruction of MRI images from non-uniform sampling and its application to intrascan motion correction in functional MRI, in: J. Benedetto, P.J.S.G. Ferreira (Eds.), Modern Sampling Theory: Mathematics and Applications, Birkhäuser, Boston, 2001.
[35] R.N. Bracewell, Strip integration in radio astronomy, Aust. J. Phys. 9 (1956) 198–217.
[36] S.W. Rowland, Computer implementation of image reconstruction formulas, in: G.T. Herman (Ed.), Image Reconstruction from Projections, Springer-Verlag, Berlin, 1979.
[37] A.C. Kak, M. Slaney, Principles of Computerized Tomographic Imaging, IEEE Press, New York, 1999.
[38] E. Kupče, R. Freeman, The radon transform: a new scheme for fast multidimensional NMR, Concepts Magn. Res. 22A (2004) 4–11.
[39] R.A. Venters, B.E. Coggins, D. Kojetin, J. Cavanagh, P. Zhou, (4,2)D Projection-reconstruction experiments for protein backbone assignment: application to human carbonic anhydrase II and calbindin D28K, J. Am. Chem. Soc. 127 (2005) 8785–8795.
[40] J. Radon, Uber die Bestimmung von Funktionen durch ihre Integralwerte längs gewisser Mannigsfaltigkeiten, Berichte über die Verhandlungen der königlich Sächsischen Gesellschaft der Wissenschaften zu Leipzig, Math.-Phys. Klasse 69 (1917) 262–277.
[41] D.J. DeRosier, A. Klug, Reconstruction of three dimensional structures from electron micrographs, Nature 217 (1968) 130–134.
[42] R.A. Crowther, D.J. DeRosier, A. Klug, The reconstruction of a three-dimensional structure from projections and its application to electron microscopy, Proc. R. Soc. London A 317 (1970) 319–340.
[43] P. Gilbert, Iterative methods for the three-dimensional reconstruction of an object from projections, J. Theor. Biol. 36 (1972) 105–117.
[44] S.R. Deans, The Radon Transform and Some of Its Applications, John Wiley, New York, 1983.
[45] F. Delaglio, S. Grzesiek, G.W. Vuister, G. Zhu, J. Pfeifer, A. Bax, NMRPipe: a multidimensional spectral processing system based on UNIX pipes, J. Biomol. NMR 6 (1995) 277–293.